PCCP

PAPER

View Article Online
View Journal

Cite this: DOI: 10.1039/d5cp03632a

Organophosphate ethyl paraoxon on Ag and Au surfaces: a density functional theory perspective

Hang Hu, †*[a] Jiří Hostaš, †*[a] Mohammad Sajjad Ghaemi, [a] Junan Lin, [a] Shiliang Wang, [a] Anguang Hu [b] and Hsu Kiang Ooi [a]

Received 20th September 2025,
Accepted 14th March 2026

DOI: 10.1039/d5cp03632a

rsc.li/pccp

Organophosphates, a class of organic compounds containing phosphorus, have garnered considerable attention due to their widespread application in agriculture. Understanding their optical properties is crucial for food safety, toxicity analysis, and early detection. In this work, the optical properties of an organophosphate containing a paraoxon moiety and its interactions with gold and silver surfaces are investigated using density functional theory. The differences between physisorption and chemisorption of ethyl paraoxon, a commonly used model organophosphate compound, on metal surfaces explain the discrepancies observed in the reported experimental Raman spectra.

Introduction

Contemporary agricultural practices commonly rely on fast-acting organophosphorus (OP) pesticides to treat crop diseases, safeguard against insects, and ensure a steady yield.[1] However, the persistent presence of pesticide residues in agricultural goods can lead to long-lasting harm to the environment and threaten human well-being.[1] In addition to being used as pesticides, the potential for malicious individuals to access weaponized OP agents, aiming to cause widespread harm, is a mounting source of concern. Recent incidents of exposure to these hazardous substances during the Syrian civil war, the Rhodesian war, the assassination attempt of a Russian dissident in the United Kingdom, and the tragic loss of young Indian children due to pesticide-contaminated lunches underscore the dangers of these harmful chemicals.[1–3]

A wide range of OP compounds can damage the nervous system by inhibiting acetylcholinesterase, resulting in an accumulation of the acetylcholine neurotransmitter at nerve synapses.[1] It is believed that this mechanism primarily contributes to the acute toxicity observed in OP-based molecules.[4] The initial symptoms of individuals exposed to these compounds are excessive salivation and seizures, which can be fatal if left untreated. However, the interaction of OP agents with acetylcholinesterase fails to explain the long-term neurological damage. Individuals exposed to trace amounts of an OP compound over an extended period of time can exhibit deficits in cognition, learning and memory, depression, and psychotic symptoms.[5] Recent mass spectroscopy studies revealed that OP compounds can interact with tyrosine residues, opening new proteins such as tubulin as potential targets.[6–10] Atomic force microscopy studies showed that OP compounds can facilitate phosphorylation of tyrosine residues which disrupts tubulin function and leads to the formation of abnormally small microtubules. This OP modification of the microtubules has also been hypothesized as a potential cause of long-term neurotoxicity.[5] However, the detailed ligand binding mechanism between OP molecules and tubulin remains unclear (Fig. 1).

Efficient detection methods are essential for food and public safety monitoring systems.[11,12] However, traditional methods for detecting OP compounds use inefficient standard analytical techniques, such as gas or liquid chromatography–mass spectrometry[13–15] and enzyme-linked immunosorbent assays.[16] Other detection approaches using metallic nanomaterials, most notably silver (Ag) and gold (Au) nanoparticles (NPs) referred to as AgNPs and AuNPs, have gained popularity.[17,18] Despite Ag and Au being noble metals, the amounts required are typically minimal, and these NPs can be produced using cost-effective

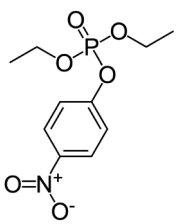

Fig. 1 Molecular structure of ethyl paraoxon with hydrogen atoms omitted for clarity.

[a] Digital Technologies Research Centre, National Research Council Canada, Toronto, ON, Canada. E-mail: hang.hu@cnrc-nrc.gc.ca, jiri.hostas@nrc-cnrc.gc.ca
[b] Suffield Research Centre, Defence Research and Development Canada, Medicine Hat, AB, Canada
† These authors contributed equally to this work.

and scalable synthesis methods.[19] As a result, Au/Ag-based NPs remain the most viable and widely accepted materials for high-performance detection applications.[20] These NPs can form aggregates in solution under specific conditions.[13,21] The NP dispersion or aggregation depends on the NP surface's response to analytes and their concentration.[22] The optical properties of NPs depend on their aggregate size and have been used to design colorimetric and fluorescence assays.[23] These methods have the advantages of high sensitivity, precision, responsiveness and repeatability, but they also require sophisticated laboratory equipment and large-scale synthesis of expensive nanomaterials,[13,23,24] which makes them unsuitable for fast on-site detection.[23–25]

To this end, surface-enhanced Raman spectroscopy (SERS) offers several key advantages: high-sensitivity, fast-detection and a simple-to-operate technique that provides detailed molecular and structural information on analytes.[25] The key to SERS sensitivity is the presence of surface hotspots, which form within nanometer-size gaps—defined as the narrow separations between adjacent metallic nanostructures—on the substrate surface.[26] It is well-established that the field enhancement intensifies markedly for gap sizes smaller than 10 nm.[27] At the hotspots the local electromagnetic field is significantly magnified and the Raman scattering signal of the adsorbed molecule can be enhanced by up to 11 orders of magnitude. There are different fabrication techniques to make nanostructured surfaces with many hotspots to improve detection sensitivity.[26,28–32] Ag- and Au-based chips or nanomaterials are often used as SERS substrates. It is relatively easy to fabricate nanometer-size gaps on the surfaces of these stable metals and utilize the gaps between Au or Ag NPs for signal enhancement.[21,26] A recent study reported an excellent OP pesticide residue detection method based on large-scale self-assembly of AuNP arrays at cyclohexane/water interfaces; the OP molecules could spontaneously localize in the gaps between the NPs, yielding excellent Raman signal enhancement.[29] In another study, a droplet with an OP molecule concentration of 10^{-9} M was placed on the AgNP surface, and post-evaporation dynamic SERS captured the Raman scattering signal from the analyte.[33]

While there is consensus on the benefits of using Ag/Au-based substrates, there are discrepancies in the reported Raman spectra of OP compounds bound to the metal surfaces, especially for ethyl paraoxon. Among the many OP compounds, substances such as dichlorvos, trichlorfon, and parathion are widely studied; however, paraoxon compounds, in particular, are commonly used as model systems in research laboratories to study the mode of action of other, more toxic pesticides and OP nerve agents.[13,34,35] It has been shown that as ethyl paraoxon nears the substrate, the current response decreases due to increased charge transfer resistance at the metal surface.[33]

Some studies have reported significant changes in the Raman shifts of the ethyl paraoxon active modes upon binding to metal surfaces.[21,26,28,36–38] In contrast, other studies suggest no Raman shift change compared to the molecular ethyl paraoxon.[16,33,39] Furthermore, some studies reported the need for the use of relatively high concentrations (exceeding 10^{-2} M) in order to successfully demonstrate detection capabilities of Au-based nanostructures[40] while others reported an impressive detection limit going down to 10^{-9} M.[33]

With theoretical chemistry emerging as an indispensable and increasingly accessible tool, a growing number of computational studies have played a crucial role in exploring the atomistic mechanisms underlying the reactivity of paraoxon moieties.[41–43] In 2022, Shukla *et al.* studied alkaline hydrolysis of paraoxon using density functional theory (DFT), confirming that the formation of 4-nitrophenol represents a key step in the reaction mechanism of paraoxon degradation.[42] In another DFT study, theoretical Raman spectra for three pesticides (thiabendazole, carbendazim, and chlorpyrifos) were calculated, which helped identify the characteristic SERS peaks in the experimental spectra.[43]

To the best of our knowledge, no theoretical studies have yet investigated the interaction of paraoxon derivatives with Ag or Au surfaces. Such studies are essential to elucidate and reconcile discrepancies observed in the experimental results and to assign the Raman shifts of ethyl paraoxon active modes upon adsorption on metal surfaces from an atomistic perspective. In this contribution, we report the first DFT study of ethyl paraoxon and the interaction of its nitrophenol fragment with metal surfaces. To contrast the effects of physisorption and chemisorption on the Raman shifts of ethyl paraoxon, the Raman spectra are calculated for the following: the molecular ethyl paraoxon, ethyl paraoxon physisorbed on an Au surface and ethyl paraoxon chemisorbed on both gold and silver surfaces.

Computational methodology

The crystal structures and phonon properties are calculated for all systems using DFT and norm-conserving pseudopotential planewave (PP-PW) basis sets as implemented in the CASTEP simulation package.[44] The Perdew–Burke–Ernzerhof (PBE) generalized gradient approximation (GGA) was used as the exchange–correlation functional.[45,46] The detailed reference configuration, kinetic energy cut-off, convergence criteria, and further details are included in the SI.

To study the interactions of ethyl paraoxon with Au and Ag surfaces, the molecule was placed on top of the metal slabs (periodic in the x–y plane) with a vacuum gap along the z direction to avoid interactions between periodic images. These surfaces are well-known to bind a variety of adsorbents through contacts with nitrogen-containing functional groups.[47,48] As previous studies have indicated a possible interaction between the paraoxon NO_2 functional group and the metal surfaces, an interaction that is also likely to produce the largest Raman shift changes, we focused on this same interaction.[24,49] To investigate physisorption, the geometry-optimized ethyl paraoxon molecule was initially placed at 4 Å above the |110| Au metal surface, with the NO_2 functional group facing the surface Au atoms. For chemisorption, the ethyl paraoxon molecule was placed at 2.8 Å above the metal |100| surfaces, with both NO_2 oxygen atoms facing a metal atom of the surface.[50]

In all adsorption calculations, all atomic positions were allowed to relax during geometry optimization. Since the ethyl paraoxon molecule is relatively rigid, a conformational search was deemed unnecessary. Testing several initial orientations was sufficient to locate the relevant local minima, which were confirmed by vibrational frequency analysis to correspond to a true minimum on the potential energy surface. The reported binding energy was defined as the energy difference between the ethyl paraoxon–metal system and the bare metal surface and free molecular ethyl paraoxon.

The Raman spectrum and scattering intensities are directly determined by the system's normal modes from vibrational frequency analysis. The determination of these normal modes is achieved by diagonalizing the force constant matrix, whose elements are obtained as the second-order derivative of the energy with respect to nuclear displacements around the optimized geometry, using a finite-difference approach.[51] The macroscopic polarizability of the system is calculated in a similar way, from which the Raman frequency and cross-section can be evaluated through space averaging.[51] The calculation of Raman intensities is more complicated.[52] By applying the double-harmonic approximation and a finite-field approach to the vibrational polarizability, the Raman-scattering intensity I^{Ram} is calculated as follows:[52]

$$I^{\mathrm{Ram}} = 45(\alpha')^2 + 7(\beta')^2, \quad (1)$$

where α' is the isotropic polarizability derivative $\frac{\mathrm{d}\alpha}{\mathrm{d}Q}$, β' represents the polarizability anisotropy derivative, and Q is the normal mode coordinate. The α' and β' can also be expressed as follows:

$$\alpha' = \frac{(\alpha'_{xx} + \alpha'_{yy} + \alpha'_{zz})}{3} \quad (2)$$

and

$$\beta'^2 = \frac{\left(\alpha'_{xx} - \alpha'_{yy}\right)^2 + \left(\alpha'_{xx} - \alpha'_{zz}\right)^2 + \left(\alpha'_{yy} - \alpha'_{zz}\right)^2 + 6\left(\alpha_{xy}'^2 + \alpha_{xz}'^2 + \alpha_{yz}'^2\right)}{2}. \quad (3)$$

The individual α_{ij} polarizability tensor components are calculated as the third-order derivative of the system energy E with respect to the normal mode coordinate Q and the external electrical field, with G_i and G_j as the electric field vectors, based on the following equation:

$$\frac{\mathrm{d}\alpha_{ij}}{\mathrm{d}Q} = \frac{\mathrm{d}^3 E}{\mathrm{d}G_i \mathrm{d}G_j \mathrm{d}Q}. \quad (4)$$

To analyze the electronic origin of adsorption-induced spectral changes, projected densities of states (PDOS) were computed by projecting the Kohn–Sham states onto orbital-resolved contributions. Also, the optical absorption (UV–vis) spectra were obtained from the frequency-dependent dielectric response of the relaxed structures within linear-response theory, and the resulting imaginary part of the dielectric function was converted to absorption features in the UV–vis range. Peak positions were interpreted by comparing the corresponding energy windows to the PDOS on occupied and unoccupied states, enabling assignment of metal-centered, ligand-centered, and charge-transfer transitions.

Results and discussion

For the molecular ethyl paraoxon, the calculated Raman shifts are in general good agreement with the experimental values with a mean absolute deviation of only 24 cm^{-1} and NO_2 symmetric stretch mode exhibiting the largest deviation of 45 cm^{-1} (see second and third columns in Table S1). The calculated Raman spectrum of molecular ethyl paraoxon is shown in Fig. 2a. The most dominant peak corresponds to the NO_2 symmetric stretch, followed by the aromatic C–C stretch. There are two additional important modes that reflect NO_2 out-of-phase stretching: the NO_2 anti-symmetric stretch with a Raman shift of 1543 cm^{-1} and the so-called NO_2 asymmetric stretch with a Raman shift of 1095 cm^{-1}. The NO_2 asymmetric stretch also involves C–H in-plane bending. It has been reported that the calculated intensity of Raman peaks can differ significantly from their experimental counterparts.[33] The calculated intensity of the Raman scattering signal depends on high-order derivatives of the system energy and is thus more prone to inaccuracy and numerical noise due to possible error propagation (small errors in the energy can result in large fluctuations of its derivatives). The discrepancy in intensity does affect the calculated Raman shifts; however, DFT-calculated molecular ethyl paraoxon reproduced experimental Raman shifts within reasonable accuracy.

Au and Ag are among the most extensively studied metal substrates. First, we analyze the interaction of ethyl paraoxon with Au metal surfaces. The calculated molecular structure of ethyl paraoxon physisorbed on the Au surface and its calculated Raman spectrum are shown in Fig. 2b. The distance between the metal surface atoms and the closest oxygen atom is approximately 4 Å. When we inspect its Raman shifts in Table S1 against the results for molecular ethyl paraoxon, we see a mean absolute differences of only 3 cm^{-1}. This indicates that physisorption does not significantly affect polarizability around the paraoxon NO_2 functional group. The calculated intensities are approximately one order of magnitude greater than those of molecular ethyl paraoxon. This increase in intensity is likely due to the metal surface increasing the overall energy and changing the system energy gradient. In this case, the normal mode vibration that significantly affects the ethyl paraoxon and metal surface distance or interaction would lead to a higher intensity. For example, the vibration of the aromatic C–C bonds will alter the distance between the ethyl paraoxon NO_2 and the Au surface, which is consistent with the dominant peak due to phenyl ring deformation (not labelled) at 1448 cm^{-1}. We also observe a smaller effect on vibrational intensities for those involving N–O vibrations.

The ethyl paraoxon can also undergo chemisorption, forming a chemical bond and creating an ethyl paraoxon–Au

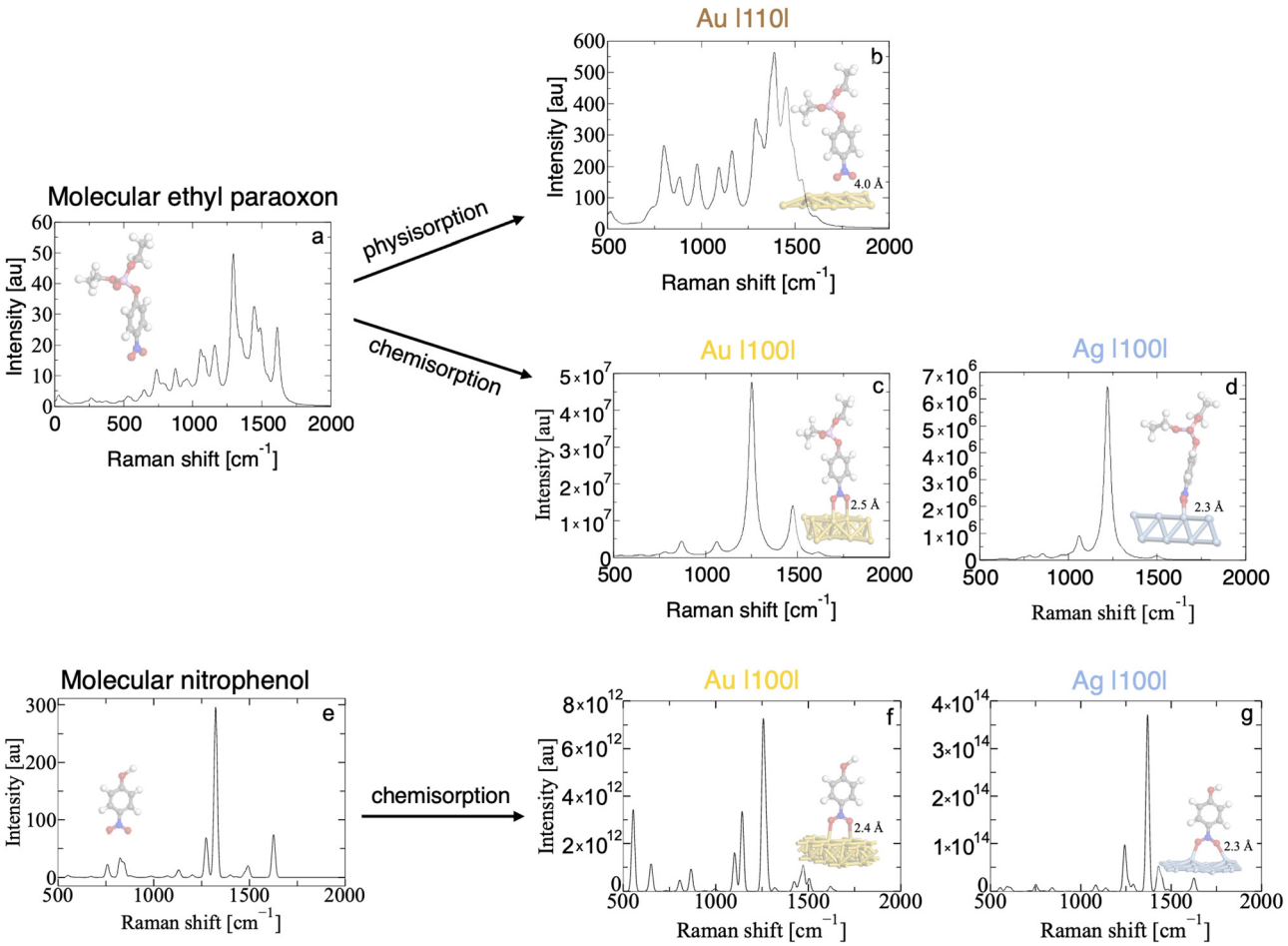

Fig. 2 Change of the Raman spectrum of molecular ethyl paraoxon (panel a) upon binding to gold and silver surfaces *via* physisorption (panel b) and chemisorption (panels c and d) and molecular nitrophenol (panel e) upon binding to gold and silver surfaces *via* chemisorption (panels f and g). To smooth the Raman peaks, the local regression is adopted and the peaks involving the NO_2 moiety and phenyl ring are assigned and labeled in Table S1, SI.

complex shown next to its Raman spectrum in Fig. 2c. Each oxygen atom of the ethyl paraoxon NO_2 functional group is bonded directly to a single gold atom. The corresponding calculated Raman shifts and changes with respect to the molecular ethyl paraoxon are listed in Table S1 and Fig. 3, respectively. All three modes involving the NO_2 group, namely scissor, symmetric stretch, and anti-symmetric stretch, exhibit redshifts. The calculated Raman shifts for the symmetric and anti-symmetric stretches are 1251 and 1487 cm^{-1}, respectively. They are both $\sim$50 cm^{-1} lower than those for molecular ethyl paraoxon, which are 1293 and 1543 cm^{-1}, respectively. The redshift for the NO_2 scissor mode is only 5 cm^{-1}, changing from 874 cm^{-1} for molecular ethyl paraoxon to 869 cm^{-1} in the chemisorbed ethyl paraoxon–Au complex. The calculated results confirm the previous experimental SERS reports of paraoxon strongly interacting with metal surfaces or nanomaterials.[21]

As in molecular ethyl paraoxon, the Raman modes of the highest intensity in the molecule chemisorbed on Au involve the NO_2 functional group, including the N–O scissor mode as well as the symmetric, asymmetric and anti-symmetric stretching modes (see Fig. 2c and 3). However, the intensities of these peaks are considerably higher than even those for ethyl paraoxon physisorbed on the Au surface. Since the intensity is proportional to the squares of the respective polarizability (see eqn 4), this is likely due to the ethyl paraoxon being closer to the Au surface, which leads to a significantly higher energy derivative and, consequently, also higher intensity peaks. With the oxygen atoms chemically bonded to the Au surface and their motion restricted, changes in vibrations involving the phenyl ring will be minor and are unlikely to significantly impact both the interaction of ethyl paraoxon with the surface and the Raman spectra in the aromatic C–C stretch region.

In SERS, silver offers high-sensitivity measurements but is susceptible to oxidation and exhibits variable stability.[53] Fig. 2d shows the molecular structure of the chemisorbed ethyl paraoxon–Ag complex, where, as in the case of gold, each oxygen atom of the NO_2 functional group is bonded to a single metal atom. The Raman spectrum for the chemisorbed ethyl paraoxon–Ag complex is shown in Fig. 2d and the selected Raman shifts are listed in Table 1. All three NO_2 Raman active modes exhibit a redshift. For the symmetric and anti-symmetric NO_2

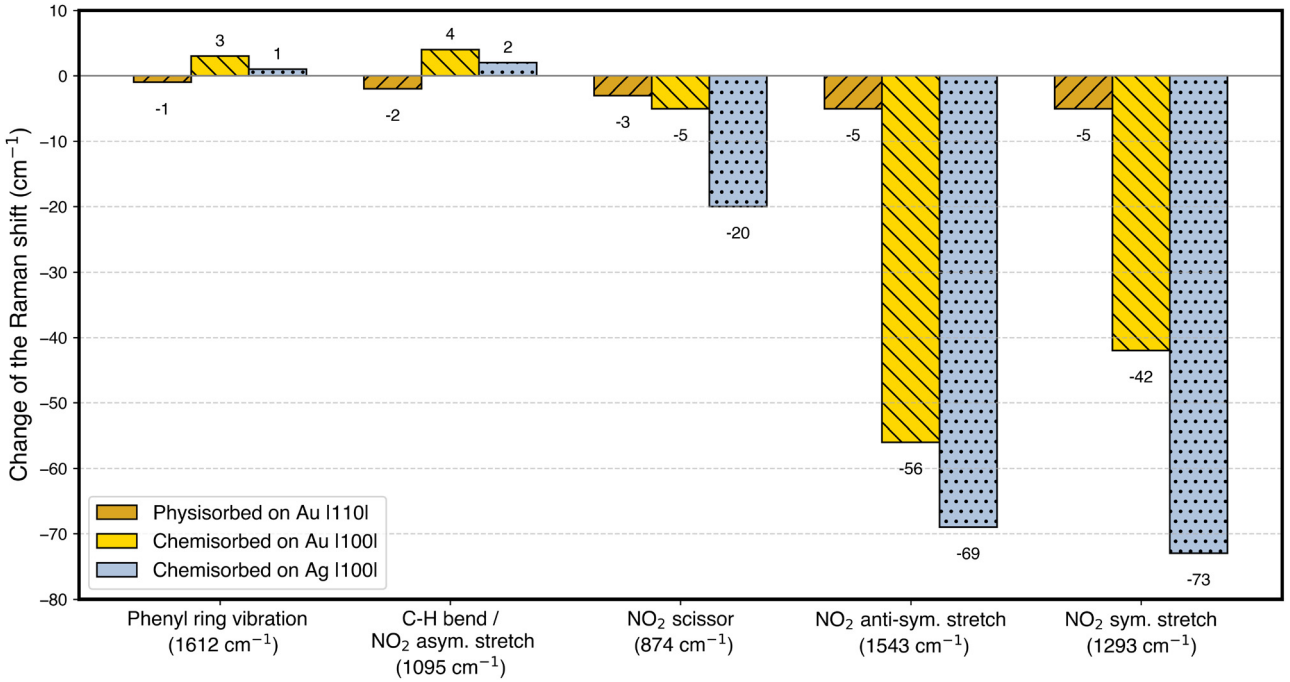

Fig. 3 Change of the Raman shifts from left to right for: phenyl ring vibration, C–H in-plane bending involving NO_2 asymmetric stretch, NO_2 scissor mode, NO_2 anti-symmetric stretch, and NO_2 symmetric stretch, respectively, upon binding to gold and silver surfaces *via* physisorption and chemisorption. Absolute values listed in parenthesis are for molecular ethyl paraoxon.

stretches, the calculated Raman shifts are 1220 and 1474 cm^{-1}, respectively, ~70 cm^{-1} lower than those of molecular ethyl paraoxon. Finally, the NO_2 scissor mode exhibits a smaller redshift of 20 cm^{-1}. The general trend in the calculated Raman shifts of the ethyl paraoxon–Ag and ethyl paraoxon–Au complexes is similar, with the ethyl paraoxon–Ag complex NO_2 redshifts being consistently larger. The overall intensity is similar to that of the ethyl paraoxon–Au complex, with the NO_2 symmetric stretch being the dominant Raman active mode. PDOS window analysis (Tables S6 and S7) confirms strong metal–NO_2 coupling in both chemisorbed complexes. Correspondingly, the UV–vis spectra exhibit multiple peaks (*e.g.*, 210 and 280–290 nm) that indicate metal d–O(p) mixing in the occupied states, consistent with NO_2-localized charge redistribution. This behavior aligns with the red shifts of NO_2 Raman modes upon chemisorption.

Table 1 presents the variations in bond lengths of key functional groups in ethyl paraoxon induced by physisorption and chemisorption on Au and Ag surfaces, alongside the associated binding energies. The average single P–O bond length in ethyl paraoxon is 1.54 Å and remains unchanged under all conditions, which is not surprising since the PO_4 group is relatively distant from the metal surface. The N–O bond length in molecular ethyl paraoxon and physisorbed ethyl paraoxon is 1.14 Å. This weak interaction explains in large part why physisorbed ethyl paraoxon does not exhibit significant changes in Raman shifts relative to molecular ethyl paraoxon.

The Raman shift depends on the polarizability of the system, which in turn depends on the dipole moment induced by normal mode vibrations. Aside from mass effects, bond length changes alone lead to different dipole moments and different Raman shifts. For ethyl paraoxon chemically bonded to the Au

Table 1 Calculated structural properties and binding energies for ethyl paraoxon, nitrophenol, and their metal-supported complexes. The length of the O–P bond remained at 1.54 Å in all formed complexes

	O–N bond [Å]	O-metal bond[a] [Å]	Binding energy [kcal mol^{-1}]	Atomic charges (in the fraction of *e*)		
				Oxygen	Nitrogen	Metal
Ethyl paraoxon	1.14	—	—	−0.28	0.36	—
Ethyl paraoxon physisorbed on Au	1.14	—	0.6	−0.30	0.34	—
Ethyl paraoxon–Au complex	1.15	2.52	16.6	−0.31	0.31	0.05
Ethyl paraoxon–Ag complex	1.18	2.32	23.7	−0.36	0.27	0.09
Nitrophenol	1.15	—	—	−0.33	0.38	—
Nitrophenol–Au complex	1.16	2.45	26.9	−0.47	0.33	0.07
Nitrophenol–Ag complex	1.16	2.35	33.4	−0.40	0.29	0.08

[a] The closest distance between the surface metal atom and oxygen.

and Ag metal surfaces, the N–O bond elongates to 1.15 and 1.18 Å, respectively. The O–metal bond length, which is defined as the closest distance between the surface atom and oxygen, is a good indicator of the ethyl paraoxon distance from the metal surface in the chemisorbed complexes. The O–Au bond length is 2.52 Å while the O–Ag bond length is 0.2 Å shorter at 2.32 Å. The shorter O–Ag bond length reflects the fact that ethyl paraoxon is closer to the Ag surface than to the Au surface, which leads to a higher binding energy and the potential of larger charge transfer to the oxygen. The binding energies of ethyl paraoxon chemisorbed on Au and Ag surfaces are 16.6 and 23.7 kcal mol^{-1}, respectively. Based on the calculated binding energies, the ethyl paraoxon–Ag complex is more stable than its Au counterpart. As expected, ethyl paraoxon physisorbed on a Au surface has the lowest binding energy of 0.6 kcal mol^{-1}.

Finally, Table 1 lists partial charges of the ethyl paraoxon NO_2 moiety atoms and the closest metal atoms. For the ethyl paraoxon–Ag complex, the oxygen atoms of the NO_2 functional group have an average charge of $-0.36e$ while the charge on nitrogen is $0.27e$. This amounts to a difference of $0.08e$ per atom from the ethyl paraoxon which supports the speculation made in earlier studies that charge transfer between the metal surface and paraoxon may be responsible for the redshifts in the Raman spectra. The degree of redshift directly correlates to the amount of charge transfer from the metal surface to the ethyl paraoxon molecule. The ethyl paraoxon–Ag complex has the most negatively charged oxygen atoms and the largest redshift of 70 cm^{-1} for the NO_2 symmetric and anti-symmetric stretch modes. The charge on the ethyl paraoxon–Au complex NO_2 oxygen atoms is $-0.31e$, which is $0.05e$ smaller in magnitude than that on the ethyl paraoxon–Ag complex. Consistent with the reduced NO_2 oxygen charges, the redshift for the ethyl paraoxon–Au complex NO_2 symmetric and anti-symmetric stretches is 20 cm^{-1} smaller than that for the ethyl paraoxon–Ag complex. Not surprisingly, the NO_2 atomic charge distribution of ethyl paraoxon physisorbed on Au ($-0.30e$ for oxygen and $0.34e$ for nitrogen) is close to that of molecular ethyl paraoxon ($-0.28e$ for oxygen and $0.36e$ for nitrogen). This partially explains why the NO_2 active modes of ethyl paraoxon physisorbed on Au do not exhibit any significant Raman shift.

The PO_4 group in ethyl paraoxon is a moderately electron-withdrawing moiety, which can compete to some extent with the nitro-group oxygens for electron density from the phenyl ring. This effect has been further evaluated by considering the interaction of nitrophenol with Au and Ag surfaces, as shown by the calculated properties in Table 1 and Table S1 in the SI. Both adsorbents exhibit the same overall trends, with stronger interactions observed when the PO_4 group is absent. The Raman shifts follow the same trends as those discussed in the case of ethyl paraoxon.

There are many conflicting reports based on experimental measurements of paraoxon Raman shifts in the presence of metal surfaces.[15,21,23,30–36] Some suggest that the paraoxon Raman active modes exhibit redshifts[15,21,23,31–33] while others indicate that the presence of the metal surface introduces no changes to the Raman shifts.[30,34–36] Our findings suggest that these discrepancies might be due to differences observed upon paraoxon undergoing physisorption and chemisorption. Previous SERS studies often compare various OPs bound to a single type of substrate, either nanostructured surfaces or nanoparticles, but the reactivity of nanomaterials is heavily influenced by their size, surface structure, and defects.[13,15,21,23,30–36] While this study provides theoretical insight into selected paraoxon–metal interactions, more systematic experimental investigations are needed to clarify the role of the metal substrate on the paraoxon Raman spectrum.

Conclusions and outlook

Surface-enhanced Raman spectroscopy is an essential technique for rapid and reliable detection of trace amounts of analytes. By adopting Ag/Au metal as substrates, the Raman scattering signal enhancement can detect OP molecules at concentrations as low as 10^{-11} M. Ethyl paraoxon is commonly used as a paradigm molecular system for OP compounds. Our DFT calculations accurately reproduce and explain Raman shifts accompanying different binding modes of ethyl paraoxon with Ag/Au surfaces. The metal surface has a limited effect on the Raman spectrum of ethyl paraoxon physisorbed on the surface of Au particles, while upon chemical binding to both Au and Ag surfaces, the ethyl paraoxon N–O Raman modes are (the most) significantly affected. This difference may help explain the discrepancy in the reported Raman spectra of paraoxon on metal substrates. In the chemisorption, the O–Ag bond is shorter than the O–Au bond, and the charge transfer from Ag to the ethyl paraoxon NO_2 functional group is greater compared to Au. This leads to a more significant redshift of the ethyl paraoxon N–O symmetric stretch, anti-symmetric stretch and scissor modes upon chemisorption to Ag relative to Au. Further experimental studies on the binding mechanism could help identify the conditions favouring physisorption *vs.* chemisorption.

To connect our work with the toxicological and biological functions of organophosphate compounds, further studies are needed to investigate the interactions of organophosphates with tubulin proteins. One promising approach is to employ semi-empirical quantum mechanics calculations using machine learning parameterized Hamiltonians, which could potentially reveal the phosphorylation mechanism of organophosphates on tyrosine residues on tubulin proteins.

Author contributions

Hang Hu: data curation (lead), formal analysis (equal), methodology (equal), validation (lead), visualization (lead), writing – original draft (equal), and writing – review & editing (supporting). Jiří Hostaš: formal analysis (equal), validation (supporting), writing – original draft (supporting), and writing – review & editing (lead). Junan Lin: writing – review & editing (supporting) and formal analysis (supporting). Mohammad Sajjad Ghaemi: formal analysis (supporting) and writing – review & editing (supporting). Shiliang Wang: methodology (supporting) and

writing – review & editing (supporting). Anguang Hu: funding acquisition (equal) and writing – review & editing (supporting). Hsu Kiang Ooi: funding acquisition (equal) and writing – review & editing (supporting).

Conflicts of interest

The authors have no conflicts to disclose.

Data availability

Additional data are available upon reasonable request.

The data that support the findings of this study are available within the article and its supplementary information (SI). Supplementary information: tables of calculated phonon frequencies and sample CASTEP simulation input. See DOI: https://doi.org/10.1039/d5cp03632a.

Acknowledgements

This project is supported by the National Research Council Canada (NRC) and the Defence Research and Development Canada (DRDC).

References

1 L. S. Deshpande, K. Phillips, B. Huang and R. J. DeLorenzo, *Neurotoxicology*, 2014, **44**, 352–357.
2 K. Than, *Organophosphates: A Common But Deadly Pesticide*, 2013, https://www.nationalgeographic.com/culture/article/130718-organophosphates-pesticides-indian-food-poisoning, Accessed: August 7, 2025.
3 C. Gould and P. Folb, *Project Coast: Apartheid's Chemical and Biological Warfare Programme*, https://unidir.org/publication/project-coast-apartheids-chemical-and-biological-warfare-programme, Accessed: August 7, 2025.
4 T. J. Dale and J. Rebek Jr., *Angew. Chem.*, 2009, **121**, 7990–7992.
5 S. Chu, M. R. Baker, G. Leong, R. J. Letcher and Q. X. Li, *Chemosphere*, 2018, **199**, 154–159.
6 O. Lockridge and L. M. Schopfer, *Chem.-Biol. Interact.*, 2010, **187**, 344–348.
7 D. Hernandez-Toledano and L. Vega, *Chem.-Biol. Interact.*, 2021, **346**, 109578.
8 W. Jiang, E. G. Duysen, H. Hansen, L. Shlyakhtenko, L. M. Schopfer and O. Lockridge, *Toxicol. Sci*, 2010, **115**, 183–193.
9 H. Grigoryan, L. M. Schopfer, C. M. Thompson, A. V. Terry, P. Masson and O. Lockridge, *Chem.-Biol. Interact.*, 2008, **175**, 180–186.
10 H. Grigoryan and O. Lockridge, *Toxicol. Appl. Pharmacol.*, 2009, **240**, 143–148.
11 A. F. Kingery and H. E. Allen, *Toxicol. Environ. Chem.*, 1995, **47**, 155–184.
12 E. J. Hulse, J. O. J. Davies, A. J. Simpson, A. M. Sciuto and M. Eddleston, *Am. J. Respir. Crit. Care Med.*, 2014, **190**, 1342–1354.
13 D. N. Kumar, A. Rajeshwari, S. A. Alex, M. Sahu, A. M. Raichur, N. Chandrasekaran and A. Mukherjee, *RSC Adv.*, 2015, **5**, 61998–62006.
14 M. K. Chai and G. H. Tan, *Food Chem.*, 2009, **117**, 561–567.
15 E. Katz and I. Willner, *Angew. Chem., Int. Ed.*, 2004, **43**, 6042–6108.
16 B. A. Makwana, D. J. Vyas, K. D. Bhatt, V. K. Jain and Y. K. Agrawal, *Spectrochim. Acta, Part A*, 2015, **134**, 73–80.
17 S. Lee, H. Xu, J. Wempner, H. Xu and J. Wen, *ACS Earth Space Chem.*, 2021, **5**, 129–135.
18 Z. Guo, X. Wu, H. Jayan, L. Yin, S. Xue, H. R. El-Seedi and X. Zou, *Food Chem.*, 2024, **434**, 137469.
19 X. Zhao and L. Li, *Appl. Surf. Sci.*, 2025, **712**, 164145.
20 M. Wang, Y. Niu, H. Peng, P. Zhang, Q. Bu, X. Song and S. Yuan, *Nanomaterials*, 2025, **15**, 1634.
21 X. Zhou, F. Zhou, H. Liu, L. Yang and J. Liu, *Analyst*, 2013, **138**, 5832–5838.
22 Z. Li, Y. Wang, Y. Ni and S. Kokot, *Sens. Actuators, B*, 2014, **193**, 205–211.
23 X. Li, H. Cui and Z. Zeng, *Sensors*, 2018, **18**, 4302.
24 A. El Alami, F. Lagarde, U. Tamer, M. Baitoul and P. Daniel, *Vib. Spectrosc.*, 2016, **87**, 27–33.
25 W. Chen, F. Long, G. Song, J. Chen, S. Peng and P. Li, *J. Raman Spectrosc.*, 2020, **51**, 611–618.
26 Y. Ma, Z. Huang, S. Li and C. Zhao, *Nanomaterials*, 2019, **9**, 426.
27 P. J. Schuck, D. P. Fromm, A. Sundaramurthy, G. S. Kino and W. E. Moerner, *Phys. Rev. Lett.*, 2005, **94**, 017402.
28 B. Ma, P. Li, L. Yang and J. Liu, *Talanta*, 2015, **141**, 1–7.
29 Y. Ma, H. Liu, M. Mao, J. Meng, L. Yang and J. Liu, *Anal. Chem.*, 2016, **88**, 8145–8151.
30 X. Yan, Y. Song, C. Zhu, H. Li, D. Du, X. Su and Y. Lin, *Anal. Chem.*, 2018, **90**, 2618–2624.
31 M. Wang, G. Shi, Y. Zhu, Y. Wang and W. Ma, *Nanomaterials*, 2018, **8**, 289.
32 H. Wang, B. Qu, H. Liu, J. Ding and N. Ren, *Sci. Total Environ*, 2018, **618**, 70–79.
33 F. Fathi, F. Lagugné-Labarthet, D. B. Pedersen and H.-B. Kraatz, *Analyst*, 2012, **137**, 4448–4453.
34 J. R. Schwierking, L. W. Menzel and E. R. Menzel, *Sci. World*, 2004, **4**, 948–955.
35 S.-W. Zhan, W.-B. Tseng and W.-L. Tseng, *Environ. Res.*, 2020, **188**, 109653.
36 H. Liu, Z. Yang, L. Meng, Y. Sun, J. Wang, L. Yang, J. Liu and Z. Tian, *J. Am. Chem. Soc.*, 2014, **136**, 5332–5341.
37 P. Li, R. Dong, Y. Wu, H. Liu, L. Kong and L. Yang, *Talanta*, 2014, **127**, 269–275.
38 S. Weng, M. Li, C. Chen, X. Gao, S. Zheng and X. Zeng, *Anal. Methods*, 2015, **7**, 2563–2567.
39 L. Zhao, C. Deng, S. Xue, H. Liu, L. Hao and M. Zhu, *Chem. Eng. J.*, 2020, **402**, 126223.

40 M. Tran, S. Roy, S. Kmiec, A. Whale, S. Martin, S. Sundararajan and S. Padalkar, *Nanomaterials*, 2020, **10**, 644.
41 R. L. De Paula, J. S. De Almeida, S. F. Cavalcante, A. S. Gonçalves, A. B. Simas, T. C. Franca, M. Valis, K. Kuca, E. Nepovimova and J. M. Granjeiro, *Molecules*, 2018, **23**, 2954.
42 C. G. Bresnahan, H. R. McAlexander, C. M. Woodley and M. K. Shukla, *Environ. Sci.: Processes Impacts*, 2022, **24**, 2249–2262.
43 M. Tao, H. Fang, X. Feng, Y. He, X. Liu, Y. Shi, Y. Wei and Z. Hong, *J. Food Qual.*, 2022, **2022**, 6947775.
44 S. J. Clark, M. D. Segall, C. J. Pickard, P. J. Hasnip, M. I. J. Probert, K. Refson and M. C. Payne, *Z. Kristallogr. - Cryst. Mater.*, 2005, **220**, 567–570.
45 J. P. Perdew, K. Burke and M. Ernzerhof, *Phys. Rev. Lett.*, 1996, **77**, 3865–3868.
46 D. Sanchez-Portal, E. Artacho and J. M. Soler, *Solid State Commun.*, 1995, **95**, 685–690.
47 N. Mahar, M. Haroon, T. A. Saleh and A. A. Al-Saadi, *J. Mol. Liq.*, 2021, **343**, 117633.
48 N. Mahar, M. Haroon, T. A. Saleh and A. A. Al-Saadi, *Surf. Interfaces*, 2022, **31**, 102059.
49 A. Zozulya, A. Zyubin and I. Samusev, *R. Soc. Open Sci.*, 2025, **12**, 242000.
50 J. R. B. Gomes and F. Illas, *Int. J. Mol. Sci.*, 2001, **2**, 211–220.
51 K. Miwa, *Phys. Rev. B:Condens. Matter Mater. Phys.*, 2011, **84**, 094304.
52 D. Porezag and M. R. Pederson, *Phys. Rev. B:Condens. Matter Mater. Phys.*, 1996, **54**, 7830–7836.
53 M. Liu, A. Bhandari, M. A. Haqqani Mohammed, D. R. Radu and C.-Y. Lai, *Appl. Nano*, 2021, **2**, 242–256.

